PNAS RESEARCH ARTICLE | MICROBIOLOGY

Metal cofactor stabilization by a partner protein is a widespread strategy employed for amidase activation

Julia E. Page[a], Meredith A. Skiba[b], Truc Do[a], Andrew C. Kruse[b], and Suzanne Walker[a,1]

Edited by Laura Kiessling, Massachusetts Institute of Technology, Cambridge, MA; received January 20, 2022; accepted May 13, 2022

Construction and remodeling of the bacterial peptidoglycan (PG) cell wall must be carefully coordinated with cell growth and division. Central to cell wall construction are hydrolases that cleave bonds in peptidoglycan. These enzymes also represent potential new antibiotic targets. One such hydrolase, the amidase LytH in *Staphylococcus aureus*, acts to remove stem peptides from PG, controlling where substrates are available for insertion of new PG strands and consequently regulating cell size. When it is absent, cells grow excessively large and have division defects. For activity, LytH requires a protein partner, ActH, that consists of an intracellular domain, a large rhomboid protease domain, and three extracellular tetratricopeptide repeats (TPRs). Here, we demonstrate that the amidase-activating function of ActH is entirely contained in its extracellular TPRs. We show that ActH binding stabilizes metals in the LytH active site and that LytH metal binding in turn is needed for stable complexation with ActH. We further present a structure of a complex of the extracellular domains of LytH and ActH. Our findings suggest that metal cofactor stabilization is a general strategy used by amidase activators and that ActH houses multiple functions within a single protein.

amidase | cell wall hydrolase | peptidoglycan | tetratricopeptide repeat

Significance

The gram-positive pathogen *Staphylococcus aureus* is a leading cause of antibiotic resistance-associated death in the United States. Many antibiotics used to treat *S. aureus*, including the beta-lactams, target biogenesis of the essential peptidoglycan cell wall. Some hydrolases play important roles in cell wall construction and are potential antibiotic targets. The amidase LytH, which requires a protein partner, ActH, for activity, is one such hydrolase. Here, we uncover how the extracellular domain of ActH binds to LytH to stabilize metals in the active site for catalysis. This work advances our understanding of how hydrolase activity is controlled to contribute productively to cell wall synthesis.

The peptidoglycan cell wall is an essential component of the cell envelope that maintains cell integrity, size, and morphology (1). Its building block, Lipid II, is synthesized inside the cell, flipped across the cell membrane, and then polymerized and cross-linked by peptidoglycan synthases from the penicillin-binding protein and SEDS (shape, elongation, division, and sporulation) families (2, 3). These enzymes have received much attention, particularly because the penicillin-binding proteins are the target of penicillin and other beta-lactams, one of the most successful classes of antibiotics in the clinic (4). However, many other enzymes, including hydrolases, are integral to building mature cell wall (5). Hydrolases are diverse enzymes that cleave bonds in peptidoglycan to allow growth, cell separation, cell wall recycling, and more (5, 6). These enzymes play important roles in bacterial physiology and present novel opportunities for antibiotic development, particularly for use in combination with beta-lactams (7–9).

LytH, a membrane-bound amidase from *Staphylococcus aureus* that acts early in cell wall synthesis, is important in controlling cell growth and division (7). It removes stem peptides from the glycan backbone of membrane-proximal peptidoglycan to control the availability of substrates for insertion of new strands (Fig. 1). When LytH is absent, cells grow excessively large and have misplaced division septa. LytH mutants also display increased sensitivity to beta-lactams, contrary to the common view that loss of hydrolase activity should be protective against beta-lactams. This sensitivity likely reflects that LytH acts on nascent peptidoglycan rather than enacting cell separation or breaking down mature cell wall (7). Other hydrolases that act at early stages of peptidoglycan synthesis show similar beta-lactam sensitivity (10, 11).

Because excessive cell wall cleavage can lead to lysis, hydrolases must be controlled. For activity, LytH requires another membrane protein called ActH. Knockouts of ActH share phenotypes of Δ*lytH* mutants, including cell size and division defects as well as oxacillin sensitivity (7). Activators of other cell wall hydrolases have been identified (12–17), but ActH does not share homology with any of them. ActH therefore provides a new opportunity to learn how amidase activity is controlled in gram-positive organisms.

In this work, we combine structural studies with biochemical and cellular experiments to elucidate how LytH and ActH interact to produce amidase activity. Beyond advancing our understanding of the LytH–ActH complex, which serves as a potential target for beta-lactam potentiators, this work reveals principles that likely extend to hydrolase activators in organisms beyond *S. aureus*.

Author affiliations: [a]Department of Microbiology, Blavatnik Institute, Harvard Medical School, Boston, MA 02115; and [b]Department of Biological Chemistry and Molecular Pharmacology, Blavatnik Institute, Harvard Medical School, Boston, MA 02115

Author contributions: J.E.P., M.A.S., T.D., A.C.K., and S.W. designed research; J.E.P., M.A.S., and T.D. performed research; J.E.P., M.A.S., T.D., A.C.K., and S.W. analyzed data; and J.E.P. and S.W. wrote the paper.

The authors declare no competing interest.

This article is a PNAS Direct Submission.

[1]To whom correspondence may be addressed. Email: suzanne_walker@hms.harvard.edu.

This article contains supporting information online at http://www.pnas.org/lookup/suppl/doi:10.1073/pnas.2201141119/-/DCSupplemental.

Published June 22, 2022.

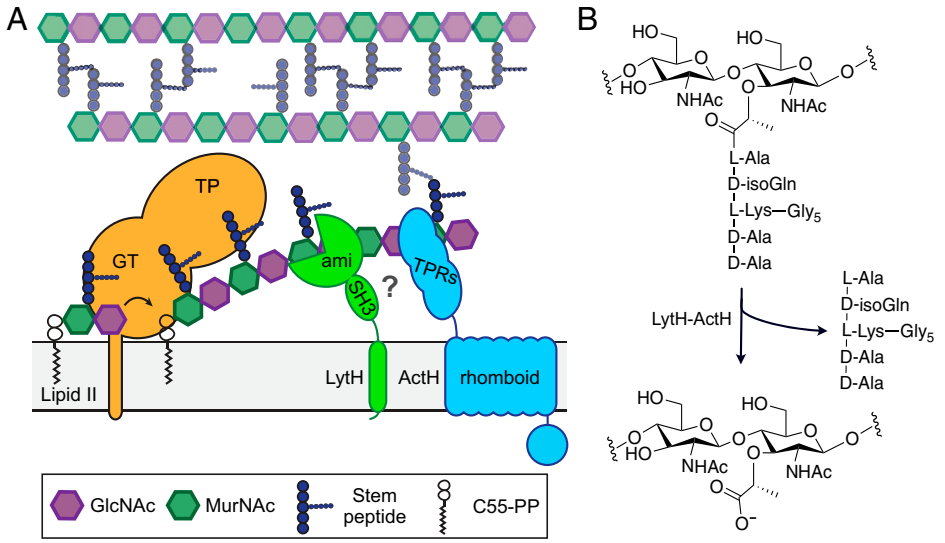

Fig. 1. How ActH stimulates the amidase activity of LytH is unknown. (*A*) Glycosyltransferases (GTs) polymerize Lipid II into glycan strands that get cross-linked into the cell wall by transpeptidases (TPs). LytH–ActH cleaves stem peptides off of uncross-linked nascent peptidoglycan, controlling the availability of stem peptides that can be used as transpeptidation substrates for insertion of new peptidoglycan strands. ActH is required for robust amidase activity of LytH, but how the two proteins interact to produce this activity is unknown. LytH contains a TM helix, an SH3 domain, and a catalytic amidase_3 domain (ami). ActH has a predicted intracellular domain of 150 amino acids, a rhomboid protease domain, and an extracellular domain with three TPRs. (*B*) The reaction catalyzed by LytH–ActH.

Results

The LytH Amidase Domain and ActH Tetratricopeptide Repeats Are Sufficient for Amidase Activity In Vitro. We first sought to determine what portions of LytH and ActH are necessary to produce amidase activity. ActH is predicted to contain a cytoplasmic domain, a seven-transmembrane helix (TM) domain with homology to the rhomboid proteases, and an extracellular domain with three tetratricopeptide repeats (TPRs). LytH contains a single transmembrane helix, an SH3 (Src homology 3) domain, and a zinc-dependent amidase domain (Figs. 1 and 2*A*). To identify which domains of these proteins are required for amidase activity, we polymerized fluorophore-labeled Lipid II, treated the peptidoglycan oligomers with pairs of truncated or full-length LytH and ActH proteins, and analyzed the products by sodium dodecyl sulfate polyacrylamide gel electrophoresis (SDS-PAGE) (Fig. 2*B*). Because the oligomers are labeled on the stem peptide, amidase activity produces tighter spacing of the peptidoglycan ladder with loss of signal intensity; a new band representing the released stem peptide also appears in the middle of the gel. Full-length LytH on its own has a small amount of activity, evidenced by some lightening of the peptidoglycan oligomer ladder and a faint band for the released stem peptide after 5 h. When ActH is added, LytH activity increases substantially (compare Fig. 2*C* lanes 4 and 7), producing a strong signal for the released stem peptide and new, low-molecular-weight ladder bands. Like full-length LytH, LytH constructs lacking either just the TM helix ($LytH_{\Delta TM}$) or both the TM helix and the SH3 domain ($LytH_{ami}$) have minimal activity in the absence of ActH. However, when combined with ActH, they produce full amidase activity (Fig. 2*C*), showing that the LytH amidase domain does not require the SH3 domain or TM helix for activity or to be activated.

We next wondered what portions of ActH are needed to stimulate LytH activity. Given that the ActH TPRs are located extracellularly in proximity to the LytH amidase domain and that TPRs are known to mediate protein–protein interactions (18), we posited that the TPRs of ActH might be responsible for its activation of LytH. When combined with either full-length LytH or the LytH amidase domain alone, the ActH TPRs ($ActH_{TPR}$) stimulated amidase activity equivalently to full-length ActH (Fig. 2*D*). The extracellular components of LytH and ActH are therefore sufficient for amidase activity in vitro.

The LytH Amidase Domain and ActH TPRs Have an Extensive Binding Interface. To understand the molecular interactions between LytH and ActH, we desired to crystallize LytH–ActH but were unsuccessful in obtaining a structure of the full-length membrane protein complex. Knowing that the soluble domains are sufficient for activity, we wondered if they might also form a stable complex that could be crystallized. We found that $LytH_{ami}$ and $ActH_{TPR}$ copurified from *Escherichia coli* as a stable 1:1 complex (Fig. 3*A*). We were able to crystallize this complex, but pathologies in the crystal lattice impeded refining the structure. We substituted a single amino acid in $LytH_{ami}$ (R245A) to disrupt a lattice contact and were able to solve the structure of the resulting crystal form to 1.8-Å resolution (Fig. 3 *B* and *C* and *SI Appendix*, Table 1). $LytH_{ami}$ R245A is active but less so than wild-type $LytH_{ami}$ (*SI Appendix*, Fig. S1). Except for in crystallographic studies, all experiments were performed with $LytH_{ami}$ retaining R245.

The structure shows the ActH TPRs binding to the base of the LytH catalytic domain on the opposite side from the active site. Each of the three TPRs demonstrates the classic helical hairpin of these structural elements (18). The TPRs are connected by short loops, forming a halfpipe with concave and convex surfaces. TPRs most commonly bind extended peptides in a near-linear conformation along the concave surface (19). The concave surface of the ActH TPR domain interacts with LytH; however, the bound region of LytH is structured and alpha-helical (Fig. 3*D*). The ActH TPRs are one of only a handful of TPR domains known to bind globular proteins (19–21).

By solvent accessibility analysis (22), LytH and ActH have a large interface with an area of 1,024 $Å^2$ stabilized by 12 hydrogen bonds and 2 salt bridges (*SI Appendix*, Fig. S2). One of these salt bridges is between LytH D264 and ActH R446 (Fig. 3*E*). To test the importance of the LytH–ActH interface observed in

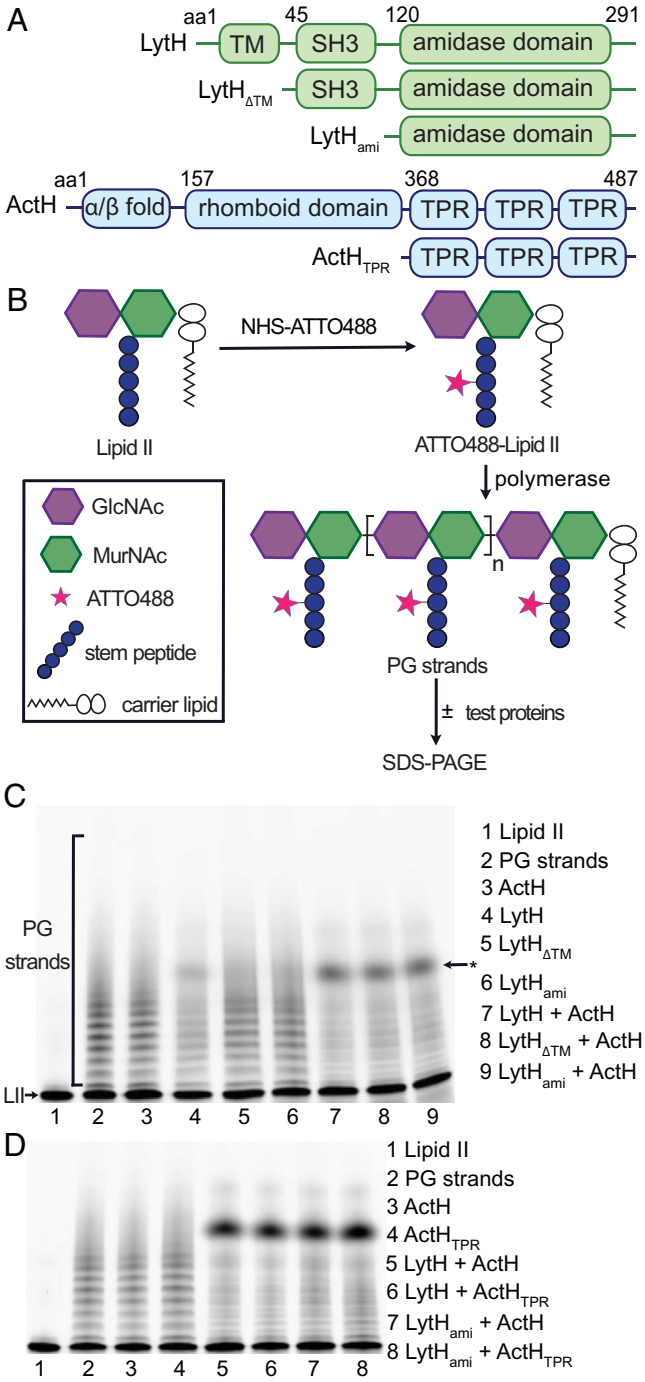

Fig. 2. The LytH amidase domain and ActH TPRs are sufficient for amidase activity in vitro. (*A*) Domain structures of LytH, ActH, and truncation mutants tested for activity. Amino acid (aa) domain boundaries are noted for the full-length proteins. Exact truncations used in particular experiments are noted in figure legends and *Methods*. (*B*) To detect amidase activity, fluorophore-labeled Lipid II is polymerized into uncross-linked peptidoglycan strands, treated with the enzyme of interest, and visualized by SDS-PAGE and fluorescence imaging. (*C*) The LytH amidase domain alone (LytH$_{ami}$, LytH[102-291]) has minimal activity but can be activated by ActH. Asterisk indicates the released fluorophore-labeled stem peptide, and LII is Lipid II. (*D*) The ActH TPRs (ActH$_{TPR}$, ActH[365-487]) are sufficient to activate LytH.

the crystal for protein complex formation, we used a simple in vitro pull-down experiment to test mutants disrupting this salt bridge. When we mixed FLAG-tagged LytH$_{ami}$ and His-tagged ActH$_{TPR}$, incubated them with FLAG resin, washed, and then eluted with FLAG peptide, both proteins were seen in the elution in approximately a 1:1 ratio. However, when LytH$_{ami}$ D264R, ActH$_{TPR}$ R446E, or ActH$_{TPR}$ R446A was combined with the wild-type version of its respective partner, no ActH$_{TPR}$ was observed in the elution (Fig. 3*F*). This interaction is also important for amidase activity. LytH$_{ami}$ D264R had no activity with or without ActH$_{TPR}$. ActH$_{TPR}$ R446E and R446A were also unable to activate LytH$_{ami}$ (Fig. 3*G*). This salt bridge is thus an important point of contact in the LytH–ActH binding interface, supporting the functional relevance of the binding orientation between ActH and LytH observed in the crystal structure.

LytH Has Four Amino Acids Coordinating Zinc, but One Is Dispensable for Zinc Binding. The LytH amidase domain consists of a twisted six-stranded beta-sheet surrounded by six alpha helices. The fold is highly conserved with solved structures of other proteins in the amidase_3 family (23–32; Protein Data Bank [PDB] ID codes 1JWQ, 3CZX, and 4RN7; PFAM ID PF01520). In our crystal structure, we observed a metal ion in the active site (initially assumed to be zinc, but see below) with an octahedral coordination sphere made up of four amino acid side chains (H128, E145, H193, and D195) and two water molecules (Fig. 3*C*). The coordinating histidines and glutamate are conserved across this amidase family, but D195 is not strictly conserved (*SI Appendix*, Fig. S3*A*). In many other amidases, this aspartate is an asparagine that is flipped out toward the solvent (*SI Appendix*, Fig. S3*B*). In these amidases, only three amino acid side chains (corresponding to H128, E145, and H193) coordinate zinc, and the remaining ligands are water molecules. Like LytH, *E. coli* AmiB and AmiC, which also require protein activators, have an aspartate that is positioned similarly to D195 to coordinate zinc (24, 25) (*SI Appendix*, Fig. S3*C*). In AmiB and AmiC, an alpha helix blocks the active site, and the activators are presumed to cause a conformational change that exposes the active site. In LytH, the active site is already exposed on the surface of the protein, raising the question of why it is inactive without ActH (*SI Appendix*, Fig. S4).

Our previous studies have shown that LytH D195 is required for catalytic activity (7). Because it is not strictly conserved, we wanted to test if it is also required for zinc binding. We copurified ActH$_{TPR}$ with wild-type or D195A LytH$_{ami}$, as well as with mutants of two of the three other zinc-coordinating residues, H128A and E145A, in buffer without added metal ions. We then used inductively coupled plasma mass spectrometry (ICP-MS) to measure levels of zinc and several other transition metals in these proteins. The wild-type sample contained predominantly zinc and iron in similar amounts, adding up to about 0.4 equivalents of metal per LytH complex. The E145A and H128A mutants had about five- to sevenfold less metal (combined iron and zinc) and two- to threefold less zinc than the wild-type complex (Fig. 4*A* and *SI Appendix*, Fig. S5 *B* and *C*). However, the D195A complex had as much zinc as the wild-type complex and also contained substantial amounts of iron (Fig. 4*A* and *SI Appendix*, Fig. S5 *B* and *C*). We conclude that D195 is not needed for stable metal binding. Consistent with this observation, in the second complex in the asymmetric unit of the crystal structure, D195 is flipped out toward the solvent, and the metal is instead coordinated by LytH D212 from the neighboring complex, which is a result of crystal packing (*SI Appendix*, Fig. S3*D*). The evident flexibility of D195 suggests that this residue may change positions upon substrate binding. More studies will be required to understand the role of D195 in catalysis.

ActH Stabilizes Metals in the LytH Active Site. We made an interesting observation while purifying the LytH$_{ami}$–ActH$_{TPR}$

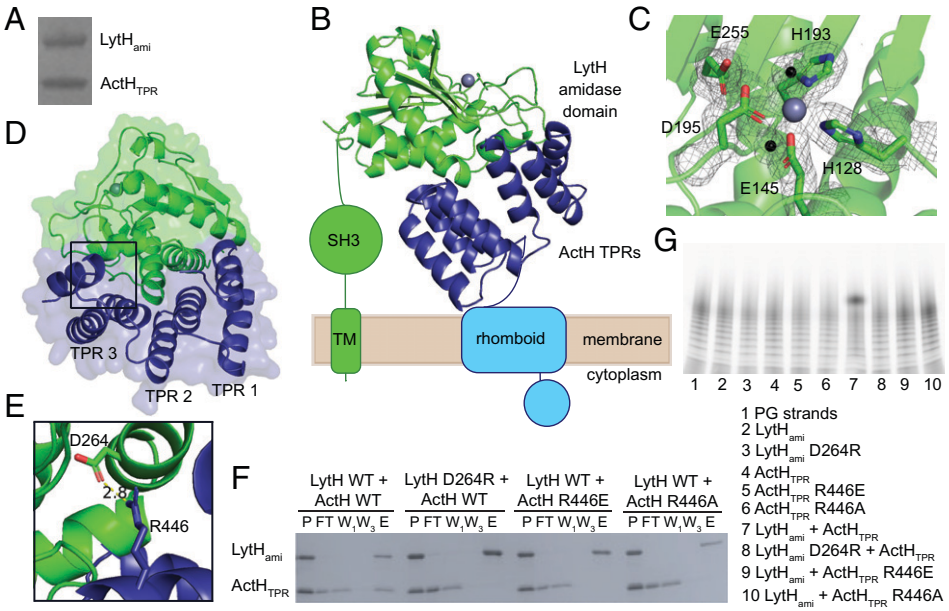

Fig. 3. Structure of the LytH amidase domain in complex with the ActH TPRs shows an extensive interface with contacts from LytH alpha helices to the TPRs. (*A*) A Coomassie-stained SDS-PAGE gel demonstrates that the LytH amidase domain (LytH[117-291]) and ActH TPRs (ActH[365-479]) copurify as a stable 1:1 complex from *E. coli*. (*B*) A crystal structure of LytH[117-291, R245A]-ActH[365-479] shows the LytH amidase domain atop the ActH TPRs. The rest of LytH and ActH are schematized. (*C*) Four amino acid side chains (H128, E145, H193, and D195) and two waters (black spheres) coordinate metal in the active site of LytH. E255 is conserved throughout amidase_3 family proteins. 2Fo-Fc electron density (gray mesh) is contoured at 1σ. (*D*) There is an extensive interface between alpha helices of the LytH amidase domain and the concave surface of the ActH TPRs. (*E*) A salt bridge forms between LytH D264 and ActH R446. (*F*) FLAG-tagged LytH$_{ami}$ (LytH[102-291]) bound to α-FLAG resin pulls down wild-type ActH$_{TPR}$ (ActH[365-487]). LytH$_{ami}$ D264R, ActH$_{TPR}$ R446E, and ActH$_{TPR}$ R446A are no longer able to stably form a complex with their wild-type partner protein. For each sample, P = preloading, FT = FLAG resin flow-through, W_1 = wash 1, W_3 = wash 3, and E = elution. WT = wild type. (*G*) Fluorescently labeled PG oligos were treated with individual proteins or combinations of LytH$_{ami}$ and ActH$_{TPR}$. Mutations in ActH and LytH that disrupt complex binding also prevent LytH activation and amidase activity.

mutant complexes for ICP-MS. When ActH$_{TPR}$ was copurified from *E. coli* with either wild-type or mutant LytH$_{ami}$ and submitted to size-exclusion chromatography (SEC), the LytH$_{ami}$ wild type and D195A complexes eluted as single peaks. However, only small peaks for the complex were seen for LytH$_{ami}$ H128A and E145A, with the majority of the protein eluting as the individual proteins (*SI Appendix*, Fig. S6). This observation suggested that LytH metal binding is necessary for stable complex formation with ActH.

We wondered whether ActH, in turn, stabilizes metal in the active site of LytH. To test this, we measured the amount of zinc and iron in purified samples of the LytH$_{ami}$–ActH$_{TPR}$ complex or individual proteins alone and found that the molar ratio of metal (combined zinc + iron) to protein was about 15-fold higher in the complex than in LytH$_{ami}$ alone (Fig. 4*B* and *SI Appendix*, S5 *B* and *C*). The LytH$_{ami}$ D195A–ActH$_{TPR}$ complex similarly had significantly more metal than LytH$_{ami}$ D195A alone (*SI Appendix*, Fig. S5*A*). Only trace amounts of metal were found in purified samples of ActH$_{TPR}$ alone. We conclude that ActH stabilizes the binding of metals in the LytH active site, and LytH metal binding in turn stabilizes the LytH–ActH interface.

LytH Can Use Iron as Well as Zinc for Catalysis. Given that we observed comparable amounts of iron and zinc in our LytH$_{ami}$–ActH$_{TPR}$ purifications without added metal, we wondered if iron is also bound in the LytH active site. To determine the metals present at the metal binding site in our crystal structure, we used anomalous scattering. Data were recorded above the K-edge for zinc (9.70 keV) and iron (7.26 keV). Both energies yielded anomalous difference electron density, indicating that both zinc and iron are found at the same position in the active site of the crystallized protein complex, though no metal was added during crystallization (*SI Appendix*, Fig. S7).

The presence of another metal in the active site of LytH led us to ask whether metals other than zinc support catalysis. We purified LytH$_{ami}$ and ActH$_{TPR}$ individually to reduce the amount of residual metal present, combined them, and treated the complex with a chelator prior to adding metals in excess. Under aerobic conditions, we observed robust amidase activity with zinc(II), cobalt(II), nickel(II), and copper(II) (*SI Appendix*, Fig. S8). We did not observe activity when we added ferrous ammonium sulfate but hypothesized that rapid oxidation to iron(III) prevented reaction. We tested iron(II) and zinc(II) again under anaerobic conditions and then found that iron(II) supported robust catalysis (Fig. 4*C*).

The ActH TPRs Are Necessary and Sufficient for LytH Activity in Cells. Knowing that the ActH TPRs are sufficient to activate LytH in vitro, we next wondered whether they would also suffice for activating LytH in cells. A knockout of *lytH* has a striking phenotype of large cells with division defects due to poorly controlled cell growth. This mutant is also particularly sensitive to the beta-lactam oxacillin. ActH mutants have similar morphological defects and increased susceptibility to oxacillin (7). We asked whether supplying just the TPRs tethered to the membrane would be sufficient to rescue these cellular defects. In addition to demonstrating sufficiency, such a result would imply that these Δ*actH* phenotypes are due to loss of LytH activity rather than loss of a function of the rhomboid or intracellular domains of ActH. We introduced several FLAG-tagged truncation mutants of ActH on single-copy integrative plasmids into a Δ*actH* or Δ*actH* Δ*lytH* background and tested growth on oxacillin. No complementation occurred for any constructs in the double-mutant background (*SI Appendix*, Fig. S9) or when a truncation lacking the TPRs was introduced into the Δ*actH* mutant (Fig. 5*A* and *SI Appendix*, Fig. S10*A*). However,

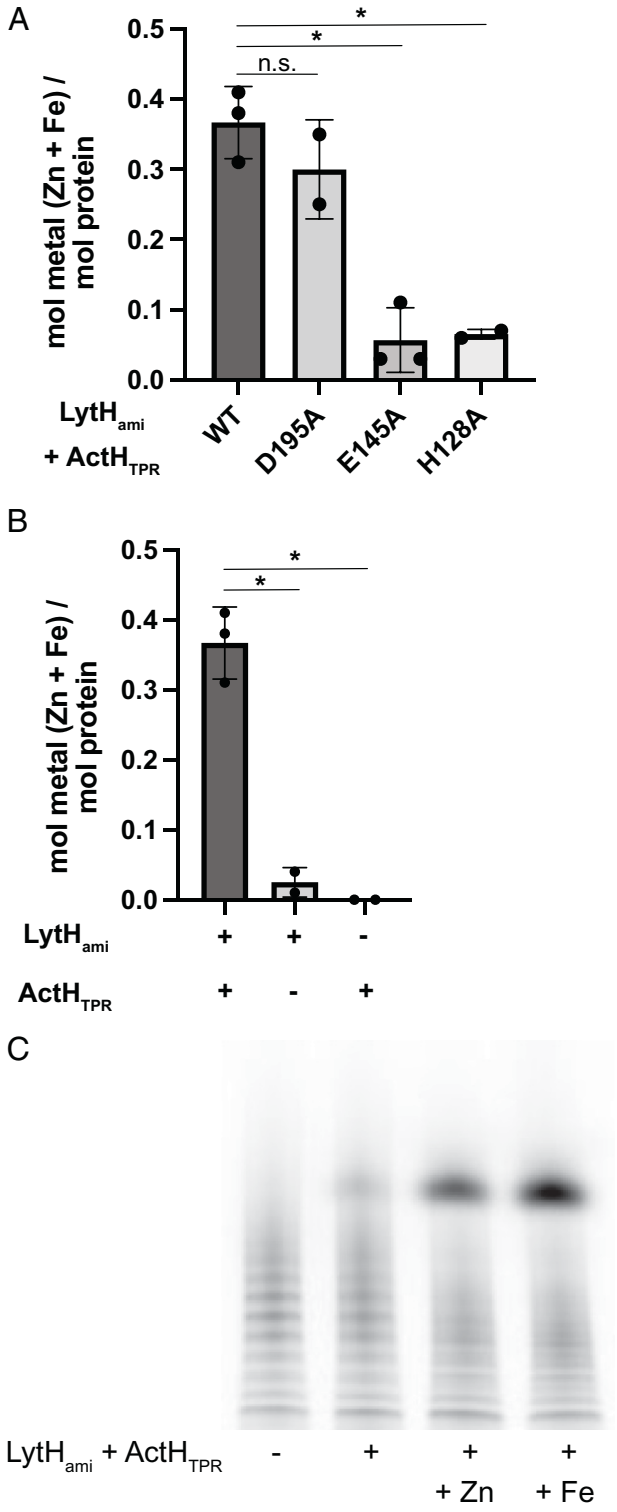

Fig. 4. ActH stabilizes zinc and iron in the LytH active site to support catalysis by either metal. (*A*) Zinc and iron were quantified in copurifications of wild-type or mutant LytH$_{ami}$ with ActH$_{TPR}$ by ICP-MS. LytH D195 is not required for metal binding, although H128 and E145 are. Each dot represents an independent purification. Each mutant was compared to the wild type by an unpaired *t* test. *$P < 0.005$. For D195A, $P = 0.3$. n.s., not statistically significant. (*B*) Zinc and iron were quantified in purifications of the LytH$_{ami}$–ActH$_{TPR}$ complex or the single proteins alone by ICP-MS. Each dot represents an independent purification. Significantly more metal is found in the complex than in LytH$_{ami}$ alone. Individual proteins were compared to the complex by unpaired *t* tests. *$P < 0.005$. (*C*) LytH$_{ami}$ and ActH$_{TPR}$ were purified independently, combined, and treated with a chelator. The protein was then added to fluorescently-labeled PG oligos in the presence of excess zinc sulfate or ferrous ammonium sulfate in an anaerobic environment. Both Zn(II) and Fe(II) can support LytH catalysis.

when the TPRs were fused to a single TM helix of the ActH rhomboid protease domain, whether the first or last helix, growth was comparable to wild type (Fig. 5*A* and *SI Appendix*, Fig. S10*A*). Even when the TPRs were expressed fused to just the signal sequence of protein A, they restored growth on oxacillin (Fig. 5*A* and *SI Appendix*, Fig. S10*A*). The chromosomally integrated FLAG-tagged proteins in all of these strains were undetectable by Western blot. To ensure that the lack of function of the construct lacking the TPRs was not due simply to poor expression, we introduced the same truncations on a plasmid with higher expression levels. All proteins could then be detected by FLAG Western blot (*SI Appendix*, Fig. S10*C*), but the construct lacking the TPRs still did not restore growth of Δ*actH* on oxacillin (*SI Appendix*, Fig. S10*B*). Western blot analysis of the construct with the TPRs fused to the protein A signal sequence showed near-complete cleavage of the TPRs from the signal sequence, suggesting that the high affinity of the TPRs for LytH may allow activation even when not tethered to the membrane (*SI Appendix*, Fig. S10*D*). These results establish that complementation depends on the presence of the hydrolase and requires only the TPRs of ActH.

We wondered if a single-pass TM–TPR construct would also rescue the morphological defects of Δ*actH*. We stained *S. aureus* cells with the membrane dye Nile red and quantified their size. A single-pass TM–TPR construct produced cells of wild-type size (Fig. 5*B* and *SI Appendix*, Fig. S11). Because only the TPRs on a single TM helix are able to restore both normal cell size and resistance to oxacillin, we have concluded that the rhomboid protease and intracellular domains of ActH are dispensable for these phenotypes. Paired with our in vitro data, these studies show that the morphological and beta-lactam susceptibility defects of Δ*actH* cells are due to loss of LytH activity and that the ActH TPRs are both sufficient and necessary to activate LytH in cells.

The LytH SH3 Domain Is Required for Activity in Cells. Like the rhomboid domain of ActH, the SH3 domain of LytH is not required for activity in vitro, so we wondered if it would also be dispensable in cells. When we introduced a LytH construct lacking the SH3 domain into a Δ*lytH* background it was not able to restore growth on oxacillin (*SI Appendix*, Fig. S13*C*), although we verified that it formed a complex with ActH and was active in vitro (*SI Appendix*, Fig. S14) and was expressed in cells (*SI Appendix*, Fig. S13*D*). The SH3 domain is thus essential for LytH activity in cells. DeepMind's AlphaFold2 (33) predicted the same binding interface between the LytH amidase domain and ActH TPRs seen in our structure and allowed us to visualize the modeled full-length complex (*SI Appendix*, Fig. S12). The extracellular complex sits atop the ActH rhomboid domain, with the SH3 domain of LytH descending on the back of the amidase domain to the single LytH TM helix. We wondered if the SH3 domain is necessary mainly as a spacer to position the catalytic domain for interaction with ActH. To test this, we replaced the native SH3 domain of LytH with either a linker or an SH3 domain from the *Bacillus subtilis* amidase YrvJ (*SI Appendix*, Fig. S13 *A* and *B*), which is also membrane-bound. All constructs were stably expressed (*SI Appendix*, Fig. S13*D*), but none was able to restore growth on oxacillin (*SI Appendix*, Fig. S13*C*). We confirmed complex formation with ActH and activity for a LytH mutant with the YrvJ SH3 domain in vitro (*SI Appendix*, Fig. S14). Our inability to complement the Δ*lytH* strain with a chimera containing an SH3 domain from another species suggests that the SH3 domain is not simply a spacer. Some bacterial SH3

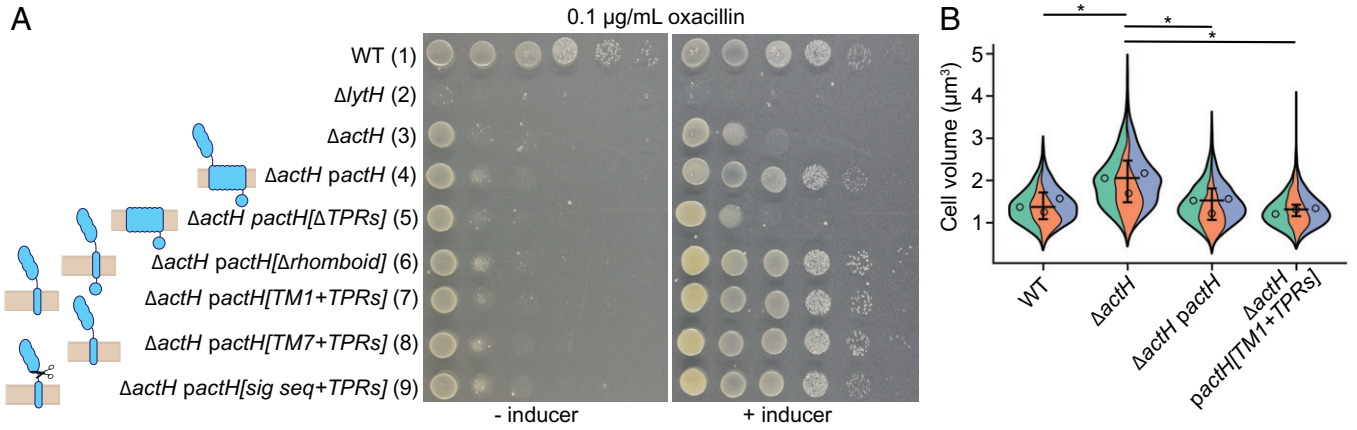

Fig. 5. The ActH TPRs are sufficient for LytH activation in cells. (*A*) *S. aureus* HG003 Δ*lytH* and Δ*actH* are both sensitive to oxacillin. This sensitivity is complemented by all ActH constructs containing the TPR domain (rows 4, 6 to 9), but not by a construct lacking the TPR domain (row 5). Strains used are HG003 (row 1) wild type, (row 2) Δ*lytH*, (row 3) Δ*actH*, (row 4) Δ*actH* p*actH*, (row 5) Δ*actH* p*actH[2-367]*, (row 6) Δ*actH* p*actH[1-178, 365-487]*, (row 7) Δ*actH* p*actH[151-178, 365-487]*, (row 8) Δ*actH* p*actH[337-487]*, and (row 9) Δ*actH* p*spa[1-38]-actH[365-487]*. All constructs were expressed from pTP63 by induction with 0.4 μM anhydrotetracycline. (*B*) *S. aureus* cells were stained with the membrane dye Nile Red, and the volumes of nondividing cells were estimated (7) and plotted as Violin SuperPlots (68). Complementation of Δ*actH* with TPR-containing constructs of ActH corrects the size defects associated with loss of LytH activity. In each plot, each color represents a biological replicate, the circles show the medians of those replicates, and the horizontal bars mark the mean with 95% confidence interval of the replicate medians. Over 300 cells were counted for each biological replicate. *P* values were determined by a one-way ANOVA followed by Tukey's tests with Bonferroni corrections. **P* < 0.05. All other pairs were not significantly different.

domains are known to bind and recognize cell wall substrates (34–37). In eukaryotes, where SH3 domains were first identified, they are found in a variety of signaling and cytoskeletal proteins and classically bind to proline-rich peptides (38, 39). Although the LytH SH3 domain does not strongly resemble SH3 domains known to bind *S. aureus* peptidoglycan (36, 40), it may nevertheless be important for *in cellulo* substrate recognition. Alternatively, it may mediate a protein–protein interaction with a yet-unidentified binding partner.

Discussion

This work reveals the mechanism underlying a class of amidase activators. First, we showed that the extracellular TPR domain of ActH activates LytH both in vitro and in cells. The rhomboid and intracellular domains of ActH are dispensable for phenotypes associated with both Δ*lytH* and Δ*actH*, suggesting that ActH has another, unknown function with temporal and spatial requirements similar to LytH activation. Next, we reported a crystal structure of a complex of the extracellular domains of LytH and ActH that shows an unusual mode of TPR binding. We further showed that ActH activates LytH at least in part by stabilizing metals in the LytH active site, a strategy which, as we discuss below, seems to be employed by activators in different structural classes.

Hydrolase activity must be carefully tuned to allow cell growth and division but avoid excessive cleavage of the essential cell wall. Bacteria employ diverse strategies to ensure that hydrolases only act in the correct time and place. These strategies include regulating hydrolase expression, modifying hydrolase substrates in the cell wall, and targeting hydrolases to particular cell wall compartments (5). Direct protein regulators of hydrolases have also been identified (10, 12–16), with the first characterized amidase activators being NlpD and EnvC, which activate the cell separation amidases AmiA/B/C in gram-negative organisms (12, 41–43). Crystal structures of AmiB and AmiC have shown they contain an alpha helix that blocks the active site and is purportedly displaced upon interaction with the activator (24, 25). LytH does not have a blocking helix. Although we were unable to crystallize the LytH amidase domain alone, the structure of LytH observed in the complex is similar to those of amidases that are functional without an activator. However, we have shown that ActH stabilizes metals in the LytH active site, presumably by inducing small conformational changes.

Recently, the *Clostridioides difficile* lipoprotein GerS was also found to stabilize zinc binding in the amidase CwlD to promote activity (32). Moreover, as with ActH and LytH, metal cofactor binding was found to be important for stable association between GerS and CwlD. GerS bears no resemblance to ActH. Instead, it is a lipoprotein tethered to diacylglycerol in the membrane and has a single extracellular domain largely composed of an antiparallel beta-sheet. That GerS and ActH, two structurally different proteins, both act by stabilizing metal binding in their respective amidases suggests that metal cofactor stabilization is a widespread strategy employed for amidase activation.

Unexpectedly, we found that LytH can use iron in its active site in place of zinc and that iron binding is also stabilized by ActH. Scattered reports show that other amidases can use metals other than zinc to promote hydrolysis (27). In one study, CwlV from *Paenibacillus polymyxa* was found to purify predominantly with zinc but also contained significant amounts of manganese. Moreover, CwlV had robust activity in the presence of either cobalt or manganese (44). To our knowledge, iron has not been reported as a cofactor in peptidoglycan amidases. However, there are examples of zinc-dependent hydrolases that can use iron(II) in place of zinc(II) to cleave amide bonds. LpxC, which catalyzes the committed step in Lipid A biosynthesis by hydrolyzing an N-acyl bond, can bind either zinc(II) or iron(II) under native conditions, and although the affinity for zinc is greater than for iron, the enzyme is more active with an iron cofactor (45). Because exchangeable intracellular iron(II) is present in greater abundance than zinc(II) under most conditions, it has been argued that iron is the dominant cofactor. Histone deacetylase 8 (HDAC8) was similarly found to use either iron or zinc and has higher activity when bound to iron (46). Although LpxC, HDAC8, and LytH have different substrates, they all cleave amide bonds. It is thus conceivable that LytH similarly makes use of different metal cofactors depending on the conditions. This versatility may bolster *S. aureus*'s ability to survive in variable environments, including during host infection when transition metals are limited (47).

We have shown that the rhomboid protease domain of ActH is dispensable for the shared phenotypes of Δ*lytH* and Δ*actH*, implying that there is no necessary interaction between the TM helix of LytH and the intramembrane domain of ActH. In contrast, the glucosaminidase SagB, which is also regulated by an intramembrane protein with homology to a family of proteases, forms close contacts through its TM helix with intramembrane helices of the protease, SpdC (10). Protein–protein interactions through membrane domains is a common theme in all cells. That ActH's hydrolase-regulating function is entirely contained in its extracellular TPR domain, yet ActH homologs with both a rhomboid domain and a TPR domain are widespread in Firmicutes (7, 48), suggests there may be some connection between the LytH-activating role of ActH and its unknown other roles. Rhomboid proteases are found in all domains of life and have important roles in eukaryotes (49), but their functions in bacteria have remained more mysterious (48–51). Some may act as chaperones because they lack key catalytic residues (52); at least one that contains catalytic residues is reported to have chaperone-like activity in addition to its proteolytic function (48). Our constructs that lack the rhomboid protease domain, yet activate LytH, now allow exploration of phenotypes specifically associated with the rhomboid domain.

An unanswered question is what purpose is served by having an activator of LytH. A standard view in the field is that cell wall hydrolase activators are required to prevent excessive cleavage of the cell wall. However, some cell wall hydrolases have intrinsic activity, and temporal or spatial mechanisms are used for regulation. For example, the membrane-bound cell wall hydrolase SagB is intrinsically active but is unable to effect peptidoglycan cleavage when SpdC is deleted, evidently because it cannot access substrate that is partially cross-linked into the cell wall matrix unless it is properly presented atop SpdC (10). Investigating the conditions under which ActH and LytH are expressed, and the levels to which they are natively expressed, could be helpful in elucidating the purpose of requiring complexation for activity and might begin to shed some light on why the LytH activation domain is found in a much larger protein with other functions.

Methods

Materials. Unless otherwise indicated, all chemicals and reagents were purchased from Sigma-Aldrich. Restriction enzymes, KOD DNA polymerase, Q5 2X Master Mix, Phusion 2X Master Mix, and T4 polynucleotide kinase were purchased from New England Biolabs. The In-fusion HD Cloning Plus kit was purchased from Takara Bio USA. Oligonucleotide primers were purchased from Integrated DNA Technologies (IDT). Culture media were purchased from Becton Dickinson. *Streptococcus pneumoniae* Δ*murMN* Lipid II was isolated from cells as described previously (53, 54). Lipid II was labeled with ATTO488 as previously described (11). *S. aureus* SgtB^{Y181D} was expressed and purified as previously reported (55). Genomic DNA was isolated using a Wizard Genomic DNA Purification kit (Promega).

Bacterial Growth Conditions. *E. coli* strains were grown with shaking at 37 °C in lysogeny broth (LB), Terrific Broth (TB), or on agarized LB plates with appropriate antibiotics. *S. aureus* strains were grown with shaking at 30 or 37 °C in tryptic soy broth (TSB) or on agarized TSB plates containing antibiotics as appropriate. Plasmids were cloned using *E. coli* NEB 10-beta cells. *E. coli* Stellar cells were used for cloning with the In-fusion HD Cloning Plus kit. The *E. coli* C43 (DE3) strain was used for overexpression of membrane-anchored proteins, and the BL21 (DE3) strain was used for overexpression of all soluble proteins. The following concentrations of antibiotics were used: carbenicillin, 100 μg/mL; chloramphenicol, 10 μg/mL; erythromycin, 10 μg/mL; kanamycin, 50 μg/mL (neomycin, 50 μg/mL was added as well for kanamycin resistant *S. aureus* strains); and tetracycline, 3 μg/mL. The bacterial strains, plasmids, and oligonucleotide primers used in this study are summarized in *SI Appendix*, Tables S2–S4. Protocols for plasmid construction can be found in *SI Appendix, Supplementary Methods*.

Protein Expression. For each soluble protein, *E. coli* BL21(DE3) containing the expression plasmid of interest was grown in 1 to 1.5 L LB supplemented with the appropriate antibiotics at 37 °C with shaking until optical density at 600 nm (OD_{600}) ∼0.6. The culture was cooled to 16 °C, and protein expression was induced by adding 500 μM isopropyl β-D-1-thiogalactopyranoside (IPTG). For each membrane-bound protein, *E. coli* C43(DE3) containing the expression plasmid of interest was grown in 1 to 1.5 L TB supplemented with appropriate antibiotics at 37 °C with shaking until OD_{600} ∼0.8. The culture was cooled to 16 °C, and protein expression was induced by adding 1 mM IPTG. Cells were harvested 18 h postinduction by centrifugation (4,000 × *g*, 10 min, 4 °C), and the pellet was stored at −80 °C.

Purification of Soluble His$_6$-Tagged Proteins. Proteins from expression constructs pTD2 and pTD3 were purified as previously described (7). For elemental analyses, protein expressed from pTD3 was purified as described here. All steps after cell lysis were performed at 4 °C. Cells were resuspended in 30 mL Buffer A (50 mM Hepes, pH 7.5, 500 mM NaCl, and 10% glycerol) supplemented with 5 mM $MgCl_2$, 1 mM Tris(2-carboxyethyl)phosphine (TCEP), 1 mg/mL lysozyme, 250 μg/mL DNase, 1 mM phenylmethylsulfonyl fluoride (PMSF), and Roche cOmplete Protease Inhibitor and stirred to homogenize. The resuspended cells were then passaged through a cell disruptor (EmulsiFlex-C5, Avestin) at 15,000 psi three times to lyse. Cell debris was removed by centrifugation (10,000 × *g*, 5 min, 4 °C), and the membrane fraction was removed by ultracentrifugation of the supernatant (119,000 × *g*, 45 min, 4 °C). The resulting supernatant was supplemented with 1 mL preequilibrated Ni-NTA resin (Qiagen) and 10 mM imidazole and stirred for 30 min at 4 °C. The sample was then loaded onto a gravity column and washed with 30 mL Buffer A containing 10 mM imidazole, 30 mL Buffer A containing 20 mM imidazole, and 30 mL Buffer A containing 40 mM imidazole. The protein was then eluted in 20 mL Buffer A containing 300 mM imidazole. The eluate was further purified by SEC with a Superdex 75 10/300 GL (for expression constructs pJP62, pJP151, and pJP152) or Superdex 200 Increase 10/300 GL (all others, pJP62 for elemental analysis) equilibrated in Buffer A. Fractions containing the target protein were concentrated by centrifugal filtration. The absorbance at 280 nm was measured using a NanoDrop One Microvolume UV-Vis Spectrophotometer (ThermoFisher Scientific), and the predicted extinction coefficient was used to calculate concentration. Protein samples were then aliquoted and stored at −80 °C.

Purification of Membrane-Bound His-Tagged Proteins. Full-length His$_6$-ActH (construct pTD52) and LytH-ActH (construct pTD51) were purified as previously described (7). Full-length LytH-His$_6$ (construct pTD42), LytHΔSH3-ActH (construct pJP174), and LytH_SH3^{YrvJ}-ActH (construct pJP173) were purified as described for His-tagged soluble proteins with the following modifications. After ultracentrifugation, the membrane fraction was collected and resuspended in 30 mL solubilization buffer (Buffer A + 1% [wt/vol] *n*-dodecyl β-D-maltoside [DDM] and 1 mM TCEP). The resulting mixture was stirred for 1 h at 4 °C before ultracentrifugation (119,000 × *g*, 35 min, 4 °C). The resulting supernatant was supplemented with 0.5 to 0.75 mL preequilibrated TALON resin (Takara Clontech) and 1 mM imidazole and stirred for 30 min at 4 °C. The sample was then loaded onto a gravity column and washed with 20 mL each of Buffer A supplemented with 2 mM imidazole/1% DDM, 4 mM imidazole/0.2% DDM, 6 mM imidazole/0.1% DDM, 8 mM imidazole/0.05% DDM, 10 mM imidazole/0.05% DDM, and 15 mM imidazole/0.05% DDM. The protein was then eluted in 10 mL Buffer A containing 0.05% DDM and 150 mM imidazole. The eluate was further purified by SEC with a Superdex 200 Increase 10/300 GL column (pTD42) or Superose 6 10/300 GL column (pJP173 and pJP174) equilibrated in Buffer A with 0.05% DDM. For constructs pJP173 and pJP174, protease inhibitors were omitted from the lysis buffer, and the TALON resin was washed up to 10 mM imidazole before elution.

Purification of Soluble FLAG-Tagged Proteins. All steps after cell lysis were performed at 4 °C. Cells were resuspended in 30 mL Buffer B (50 mM Hepes, pH 7.5, 150 mM NaCl, and 10% glycerol) supplemented with 5 mM $MgCl_2$, 1 mg/mL lysozyme, 250 μg/mL DNase, and 1 mM PMSF and stirred to homogenize. The resuspended cells were then passaged through a cell disruptor

(EmulsiFlex-C5, Avestin) at 15,000 psi three times to lyse. Cell debris was removed by centrifugation (10,000 × *g*, 5 min, 4 °C), and the membrane fraction was removed by ultracentrifugation of the supernatant (119,000 × *g*, 45 min, 4 °C). The resulting supernatant was then loaded onto a gravity column with 1 mL α-FLAG G1 affinity resin (Genscript), and the flow through was passed through the column four more times. The resin was washed three times with 15 mL of Buffer B, and the protein was eluted with 10 mL of Buffer A supplemented with 0.2 mg/mL FLAG peptide (Genscript). The eluate was further purified by SEC with a Superdex 200 Increase 10/300 GL equilibrated in Buffer A. Fractions containing the target protein were concentrated by centrifugal filtration. The absorbance at 280 nm was measured using a NanoDrop One Microvolume UV-Vis Spectrophotometer (ThermoFisher Scientific), and the predicted extinction coefficient was used to calculate concentration. Protein samples were then aliquoted and stored at −80 °C.

In-Gel Detection of Amidase Activity. ATTO488-labeled Lipid II (1.4 μM) was polymerized with 1.8 μM $SgtB^{Y181D}$, a monofunctional peptidoglycan glycosyltransferase with impaired processivity (55), in 1.1× reaction buffer [1× buffer = 50 mM Hepes, pH 7.5, 10 mM $CaCl_2$, 60 μM $Zn(OAc)_2$, and 15% dimethyl sulfoxide (DMSO)] at room temperature for 2 h. The polymerization reaction was heat-quenched at 95 °C for 5 min. After cooling, the digestion reaction was set up by adding 1 μL of 5 μM enzyme to 9 μL of the polymerization reaction product (total volume 10 μL). For reactions testing pairs of independently purified proteins (LytH + ActH), mixes containing 5 μM of each protein were first prepared and incubated on ice for 20 min before addition to the polymerization reaction product. After incubating the reaction mixtures at room temperature for 5 h, the reactions were quenched by adding 10 μL 2× Laemmli sample buffer (Bio-Rad). The samples were then loaded onto a 4 to 20% Mini-PROTEAN TGX Precast Protein gel (Bio-Rad) and run at 180 V. The gels were imaged using a Typhoon FLA 7000 imager.

Metal Dependence Activity Assays. A 5 μM stock of $LytH_{ami}$ (construct pTD3) + $ActH_{TPR}$ (construct pJP62) was prepared in 50 mM Hepes, pH 7.5, and 500 μM ethylenediaminetetraacetic acid (EDTA) and incubated on ice for 30 min. ATTO488-labeled Lipid II (1.6 μM) was polymerized with 2 μM $SgtB^{Y181D}$ in 1.25× reaction buffer (1× buffer = 50 mM Hepes, pH 7.5, 500 μM EDTA, and 15% DMSO) at room temperature for 2 h. The polymerization reaction was heat-quenched at 95 °C for 5 min. After cooling, the cleavage reactions were set up by adding 1 μL of 10 mM metal sulfate of interest and 1 μL of 5 μM protein mix to 8 μL of the polymerization reaction. After incubating the reaction mixtures at room temperature for 5 h, the reactions were quenched by adding 10 μL 2× Laemmli sample buffer (Bio-Rad). The samples were then loaded onto a 4 to 20% Mini-PROTEAN TGX Precast Protein gel (Bio-Rad) and run at 180 V. The gels were imaged using a Typhoon FLA 7000 imager. For experiments in an anaerobic environment, the polymerization was first performed on the benchtop under room air. All materials including solid ferrous ammonium sulfate were then brought into an anaerobic chamber and equilibrated for 1 h before beginning the cleavage reactions. A fresh ferrous ammonium sulfate solution was prepared just before use.

Crystallization and Structure Determination. pJP85 was transformed into BL21 cells, and LytH[117-291]-ActH[365-479] was expressed and purified as described for His-tagged soluble proteins except that the final protein was exchanged into 50 mM Hepes, pH 7.5 with 150 mM NaCl on the Superdex200 Increase 10/300 GL column. Final protein was aliquoted and flash-frozen. Crystals were obtained in a 1:1 ratio of 12.6 mg/mL protein solution to 0.17 M sodium acetate, 0.085 M Tris·HCl, pH 8.5, 25.5% (wt/vol) PEG4000, and 15% (vol/vol) glycerol after 1 to 2 d at 20 °C. Crystals were harvested with nylon loops and then flash-cooled in liquid nitrogen.

Diffraction data were collected at 1.033 Å and 100 K at the Advanced Photon Source GM/CA beamline 23ID-B. Data were collected at 1° per s with 10-fold attenuation and 0.2° oscillation range. Efforts to solve the structure from this data revealed overlapping lattice patterns from twinned crystals, and the data could not be deconvoluted. Preliminary molecular replacement solutions using Phaser (56) through the Phenix Software Suite (57) with an amidase from *C. difficile* (PDB ID code 4RN7) as a search model demonstrated a trimer forming between three units of LytH, with interactions between helices spanning residues 179 to 185 and 242 to 247 on one subunit and a loop from residues 196 to 203 on the other. In order to disrupt this interaction and force the protein to crystallize in a different lattice, we prepared a series of constructs with mutations in these regions, ultimately solving the structure of LytH[117-291, R245A]-ActH[365-479].

pJP107 was transformed into BL21 cells, and LytH[117-291, R245A]-ActH[365-479] was expressed and purified as described for His-tagged proteins except that the final protein was exchanged into 50 mM Hepes, pH 7.5 with 150 mM NaCl on the Superdex200 Increase 10/300 GL column. Final protein was aliquoted and flash-frozen. Crystals were obtained in a 2:1 ratio of 12.6 mg/mL protein solution to 0.1 M NH_4NO_3, pH 6.3, and 22% (wt/vol) PEG3350 after 3 to 7 d at 20 °C. Crystals were harvested with nylon loops after cryoprotection in 0.1 M NH_4NO_3, pH 6.3, 22% (wt/vol) PEG3350, and 15% glycerol and then flash-cooled in liquid nitrogen.

Diffraction data were collected at 1.033 Å and 100 K at the Advanced Photon Source GM/CA beamline 23ID-D. Data were collected at 1° per s with 10-fold attenuation and 0.2° oscillation range. Data were processed with XDS (58). A complete dataset was obtained from one crystal and processed in space group $P22_12_1$. The structure was solved by molecular replacement using Phaser (56) through the Phenix Software Suite (57) using a *C. difficile* amidase (PDB ID code 4RN7) as a search model (59). A model of LytH and ActH was built with Phenix AutoBuild (60). Iterative rounds of model building and refinement were carried out using Coot (61) and Phenix.refine (62) with automated translation/liberation/screw group selection. Structures were validated with MolProbity (63). Figures were prepared using PyMOL (PyMOL Molecular Graphics System Version 2.3.4; Schrodinger, LLC). All structural biology software was accessed through SBGrid (64). The protein interface was analyzed using the Protein Interfaces, Surfaces and Assemblies (PISA) service at the European Bioinformatics Institute (https://www.ebi.ac.uk/pdbe/prot_int/pistart.html). AlphaFold2 models were generated using ColabFold (65).

To examine the identity of the metal in the active site of LytH we collected Friedel-pair data at X-ray energies of 9.70 and 7.26 keV. Data for isomorphous crystals was processed with XDS and phased through rigid-body refinement in Refmac5 (66).

In Vitro Pull-Down Binding Assay. Pairs of FLAG-tagged LytH proteins and His-tagged ActH proteins were mixed 1:1 at a final concentration of 11 μM for each and incubated on ice for 10 min (P, preloading). This mix (16 μL) was then loaded onto 15 μL of α-FLAG G1 resin (Genscript) preequilibrated in FLAG resin buffer (50 mM Hepes, pH 7.5, 150 mM NaCl, and 10% glycerol) in a microspin column (Pierce), and the flow-through was collected. The resin was then washed three times with 2 column volumes (CVs) of FLAG resin buffer each time, incubating on ice for 5 min with each wash before collecting. The protein was then eluted with 1 CV of FLAG resin buffer supplemented with 0.2 mg/mL FLAG peptide (Genscript) after incubating with the elution buffer for 5 min on ice. A 5× Laemmli buffer was added to each sample, and the samples were then loaded onto a 4 to 20% Midi-PROTEAN TGX Precast Protein gel (Bio-Rad) and run at 180V. The gel was stained with Instant Blue (Abcam) and imaged.

Elemental Analyses. SEC-purified proteins at 20 μM in 50 mM Hepes, pH 7.5, 500 mM NaCl, and 10% glycerol were diluted 7× in water and analyzed by ICP-MS (8900; Agilent) in helium mode at the Dartmouth Trace Element Analysis Core.

***S. aureus* Strain Construction.** To construct strains containing pTP63 plasmids, the plasmids were first electroporated into TD011, and transformants were selected on tryptic soy agar (TSA) supplemented with 10 μg/mL chloramphenicol. pTP63 constructs were then transduced into strain TD177 to produce strains JP299, JP331, JP332, JP334, JP335, and JP416 and into strain TD178 to produce strains JP425, JP426, JP427, JP428, JP429, and JP431.

To construct strains containing ActH or its truncations on pLOW plasmids, the plasmids were first electroporated into RN4220 wild type, and the transformants were selected on TSA supplemented with 10 μg/mL erythromycin. pLOW constructs were then transduced into strain TD177 to produce strains JP367, JP368, JP373, JP374, JP375, and JP432.

To construct strains containing pLOW plasmids in a Δ*lytH::kan*^{R} background, the plasmids were isolated from *E. coli* DC10B and then directly electroporated into TD024 to produce strains TD156, JP391, JP392, JP400, and JP401.

Spot Dilution Assays. *S. aureus* cultures in TSB with antibiotics as appropriate were grown overnight at 30 °C with aeration. Overnight cultures were diluted 1:100 into fresh TSB without antibiotics and grown to midlog phase. The cultures were normalized, five 10-fold dilutions were prepared in TSB, and 5 μL of each dilution were spotted onto TSA plates with or without 0.1 μg/mL oxacillin and inducer. Plates were incubated overnight at 37 °C. A Nikon D3400 DSLR camera fitted with an AF-S Micro-Nikkor 40 mm 1:2.8G lens was used to take pictures of the plates.

α-FLAG Western Blots. *S. aureus* strains were inoculated in TSB with antibiotics as appropriate and the cultures were grown at 30 °C overnight with aeration. Overnight cultures were diluted 1:100 into fresh TSB with or without 1 mM IPTG and grown for 3.5 h with aeration at 30 °C. For strains containing pLOW constructs, TSB was supplemented with erythromycin. For cellular pellet fractions, the cultures were normalized, harvested, and lysed in 1× PBS, pH 7.4, supplemented with 100 μg/mL lysostaphin, 20 μg/mL DNase, and 5 mM $MgCl_2$ with incubation at 37 °C for 1 h. Laemmli buffer was then added, and the samples were incubated at 37 °C for an additional 30 min. For supernatant fractions, the cultures were normalized and spun down at 17,000 × *g* for 5 min at 4 °C. The supernatant was then added to 1/10 its volume of 100% trichloroacetic acid, vortexed, and incubated on ice for 1 h before collecting the pellet (17,000 × *g*, 10 min, 4 °C). The pellet was washed twice with 1 mL ice-cold acetone, air-dried, resuspended in 1× PBS with Laemmli buffer, and boiled for 5 min. Samples were then loaded onto a 4 to 20% PROTEAN TGX Precast Protein gel (Bio-Rad) and run at 180 V, transferred to a nitrocellulose membrane (Bio-Rad), and blocked in 1× TBST containing 5% Blotting Grade Blocker (Bio-Rad) for 1 h at room temperature. Membranes were then blotted with 1:2,000 α-FLAG M2-HRP (Sigma-Aldrich A8592) in TBST with 5% Blotting Grade Blocker for 1 h at room temperature, washed with TBST, and exposed with ECL reagent (Pierce).

Microscopy Analysis of *S. aureus* Cells. *S. aureus* cultures were grown overnight at 30 °C in TSB with antibiotics as appropriate. The overnight cultures were then diluted to a starting OD_{600} of 0.02 in 3 mL TSB with 0.4 μM anhydrotetracycline, grown at 37 °C with aeration to midlog phase, and normalized. Cells (1 mL normalized culture) were then labeled with 5 μg/mL Nile red for 5 min at 37 °C with shaking (500 rpm). The cells were pelleted (4,000 × *g*, 2 min), most of the supernatant was removed, and the cells were resuspended in the remaining supernatant (about 50 μL). Cells were spotted onto a thin 2% agarose pad prepared in 1× PBS, pH 7.4, covered with a no. 1.5 coverslip, and sealed with Valap (equal weights of petroleum jelly, lanolin, and paraffin). Bright-field, phase-contrast, and wide-field epifluorescence microscopy images were obtained using a Nikon Ti inverted microscope fitted with a custom-made cage incubator set at 30 °C, a Nikon motorized stage with an OkoLab gas incubator and a slide insert attachment, either an Andor Zyla 4.2 Plus sCMOS or a Hamamatsu Orca Flash 4.0 V3 camera, Lumencore SpectraX LED Illumination, Plan Apo lamba ×100/1.45 Oil Ph3 DM objective lens, and Nikon Elements 4.30 acquisition software. The microscope was fitted with a 49008 Chroma ET filter cube for detecting Nile red. Exposure times for Nile red labeling were 20 to 80 ms. Images were analyzed using Fiji (67) and MATLAB scripts developed in-house. *S. aureus* cell volumes were estimated using StaphSizer as previously described (7). Only cells without a visible septum were included for this analysis. Data were presented as Violin SuperPlots (68).

Data Availability. X-ray crystallography data have been deposited in Protein Data Bank (ID code 7TJ4) (69). All other study data are included in the article and/or *SI Appendix*.

ACKNOWLEDGMENTS. We thank Brian Jackson at the Dartmouth Trace Element Analysis Core for help with the elemental analyses. We thank the Microscopy Resources on the North Quad (MicRoN) facility at Harvard Medical School for their training and support. We thank the staff at Advanced Photon Source GM/CA beamlines for support of X-ray data collection. GM/CA@APS is funded by the National Cancer Institute (ACB-12002) and the National Institute of General Medical Sciences (AGM-12006, P30GM138396). The Eiger 16M detector at GM/CA-XSD was funded by NIH grant S10 OD012289. Portions of this research were conducted at the Advanced Photon Source, a US Department of Energy (DOE) Office of Science User Facility operated for the DOE Office of Science by Argonne National Laboratory under contract DE-AC02-06CH11357. SBGrid provided structural biology software support. We acknowledge Bailey Plaman for preliminary work on LytH–ActH binding assays during her rotation, Marco Jost for use of his anaerobic chamber, and Liz Nolan and Theodore Betley for helpful discussions of metalloenzymes. Funding for this work was provided by NIH grants R01 AI139011, R01 AI148752, and R01 GM076710 to S.W. and T32 GM007753 and F30 AI156972 to J.E.P., NSF grant DGE1144152 to T.D., and a Merck Postdoctoral Fellowship from the Helen Hay Whitney Foundation to M.A.S.

1. M. Rajagopal, S. Walker, Envelope structures of gram-positive bacteria. *Curr. Top. Microbiol. Immunol.* **404**, 1–44 (2017).
2. H. Cho *et al.*, Bacterial cell wall biogenesis is mediated by SEDS and PBP polymerase families functioning semi-autonomously. *Nat. Microbiol.* **1**, 16172 (2016).
3. A. Taguchi *et al.*, FtsW is a peptidoglycan polymerase that is functional only in complex with its cognate penicillin-binding protein. *Nat. Microbiol.* **4**, 587–594 (2019).
4. E. Sauvage, F. Kerff, M. Terrak, J. A. Ayala, P. Charlier, The penicillin-binding proteins: Structure and role in peptidoglycan biosynthesis. *FEMS Microbiol. Rev.* **32**, 234–258 (2008).
5. T. Do, J. E. Page, S. Walker, Uncovering the activities, biological roles, and regulation of bacterial cell wall hydrolases and tailoring enzymes. *J. Biol. Chem.* **295**, 3347–3361 (2020).
6. W. Vollmer, B. Joris, P. Charlier, S. Foster, Bacterial peptidoglycan (murein) hydrolases. *FEMS Microbiol. Rev.* **32**, 259–286 (2008).
7. T. Do *et al.*, Staphylococcus aureus cell growth and division are regulated by an amidase that trims peptides from uncrosslinked peptidoglycan. *Nat. Microbiol.* **5**, 291–303 (2020).
8. D. Korsak, S. Liebscher, W. Vollmer, Susceptibility to antibiotics and β-lactamase induction in murein hydrolase mutants of Escherichia coli. *Antimicrob. Agents Chemother.* **49**, 1404–1409 (2005).
9. D. A. Dik *et al.*, Slt, MltD, and MltG of Pseudomonas aeruginosa as targets of bulgecin A in potentiation of β-lactam antibiotics. *ACS Chem. Biol.* **14**, 296–303 (2019).
10. K. Schaefer *et al.*, Structure and reconstitution of a hydrolase complex that may release peptidoglycan from the membrane after polymerization. *Nat. Microbiol.* **6**, 34–43 (2021).
11. A. Taguchi, J. E. Page, H. T. Tsui, M. E. Winkler, S. Walker, Biochemical reconstitution defines new functions for membrane-bound glycosidases in assembly of the bacterial cell wall. *Proc. Natl. Acad. Sci. U.S.A.* **118**, e2103740118 (2021).
12. T. Uehara, K. R. Parzych, T. Dinh, T. G. Bernhardt, Daughter cell separation is controlled by cytokinetic ring-activated cell wall hydrolysis. *EMBO J.* **29**, 1412–1422 (2010).
13. D. Mavrici *et al.*, Mycobacterium tuberculosis FtsX extracellular domain activates the peptidoglycan hydrolase, RipC. *Proc. Natl. Acad. Sci. U.S.A.* **111**, 8037–8042 (2014).
14. L.-T. Sham, S. M. Barendt, K. E. Kopecky, M. E. Winkler, Essential PcsB putative peptidoglycan hydrolase interacts with the essential FtsXSpn cell division protein in Streptococcus pneumoniae D39. *Proc. Natl. Acad. Sci. U.S.A.* **108**, E1061–E1069 (2011).
15. O. R. Diaz, C. V. Sayer, D. L. Popham, A. Shen, *Clostridium difficile* lipoprotein GerS is required for cortex modification and thus spore germination. *MSphere* **3**, e00205–e00218 (2018).
16. C. K. Gurnani Serrano *et al.*, ActS activates peptidoglycan amidases during outer membrane stress in Escherichia coli. *Mol. Microbiol.* **116**, 329–342 (2021).
17. B. E. Rued *et al.*, Structure of the large extracellular loop of FtsX and its interaction with the essential peptidoglycan hydrolase PcsB in Streptococcus pneumoniae. *MBio* **10**, e02622-18 (2019).
18. L. D. D'Andrea, L. Regan, TPR proteins: The versatile helix. *Trends Biochem. Sci.* **28**, 655–662 (2003).
19. A. Perez-Riba, L. S. Itzhaki, The tetratricopeptide-repeat motif is a versatile platform that enables diverse modes of molecular recognition. *Curr. Opin. Struct. Biol.* **54**, 43–49 (2019).
20. J. Yang *et al.*, Molecular basis for TPR domain-mediated regulation of protein phosphatase 5. *EMBO J.* **24**, 1–10 (2005).
21. K. Lapouge *et al.*, Structure of the TPR domain of p67phox in complex with Rac.GTP. *Mol. Cell* **6**, 899–907 (2000).
22. E. Krissinel, K. Henrick, Inference of macromolecular assemblies from crystalline state. *J. Mol. Biol.* **372**, 774–797 (2007).
23. F. M. Büttner, M. Renner-Schneck, T. Stehle, X-ray crystallography and its impact on understanding bacterial cell wall remodeling processes. *Int. J. Med. Microbiol.* **305**, 209–216 (2015).
24. D. C. Yang, K. Tan, A. Joachimiak, T. G. Bernhardt, A conformational switch controls cell wall-remodelling enzymes required for bacterial cell division. *Mol. Microbiol.* **85**, 768–781 (2012).
25. M. Rocaboy *et al.*, The crystal structure of the cell division amidase AmiC reveals the fold of the AMIN domain, a new peptidoglycan binding domain. *Mol. Microbiol.* **90**, 267–277 (2013).
26. D. M. Prigozhin, D. Mavrici, J. P. Huizar, H. J. Vansell, T. Alber, Structural and biochemical analyses of Mycobacterium tuberculosis N-acetylmuramyl-L-alanine amidase Rv3717 point to a role in peptidoglycan fragment recycling. *J. Biol. Chem.* **288**, 31549–31555 (2013).
27. A. Kumar *et al.*, The structure of Rv3717 reveals a novel amidase from Mycobacterium tuberculosis. *Acta Crystallogr. D Biol. Crystallogr.* **69**, 2543–2554 (2013).
28. F. M. Büttner, K. Faulhaber, K. Forchhammer, I. Maldener, T. Stehle, Enabling cell-cell communication via nanopore formation: Structure, function and localization of the unique cell wall amidase AmiC2 of Nostoc punctiforme. *FEBS J.* **283**, 1336–1350 (2016).
29. A. Usenik *et al.*, The CWB2 cell wall-anchoring module is revealed by the crystal structures of the clostridium difficile cell wall proteins Cwp8 and Cwp6. *Structure* **25**, 514–521 (2017).
30. I. P. Korndörfer *et al.*, The crystal structure of the bacteriophage PSA endolysin reveals a unique fold responsible for specific recognition of Listeria cell walls. *J. Mol. Biol.* **364**, 678–689 (2006).
31. M. J. Mayer, V. Garefalaki, R. Spoerl, A. Narbad, R. Meijers, Structure-based modification of a Clostridium difficile-targeting endolysin affects activity and host range. *J. Bacteriol.* **193**, 5477–5486 (2011).
32. C. Alves Feliciano, B. E. Eckenroth, O. R. Diaz, S. Doublié, A. Shen, A lipoprotein allosterically activates the CwlD amidase during Clostridioides difficile spore formation. *PLoS Genet.* **17**, e1009791 (2021).
33. J. Jumper *et al.*, Highly accurate protein structure prediction with AlphaFold. *Nature* **596**, 583–589 (2021).

34. C. P. Ponting, L. Aravind, J. Schultz, P. Bork, E. V. Koonin, Eukaryotic signalling domain homologues in archaea and bacteria. Ancient ancestry and horizontal gene transfer. *J. Mol. Biol.* **289**, 729–745 (1999).
35. T. Baba, O. Schneewind, Target cell specificity of a bacteriocin molecule: A C-terminal signal directs lysostaphin to the cell wall of Staphylococcus aureus. *EMBO J.* **15**, 4789–4797 (1996).
36. J. Z. Lu, T. Fujiwara, H. Komatsuzawa, M. Sugai, J. Sakon, Cell wall-targeting domain of glycylglycine endopeptidase distinguishes among peptidoglycan cross-bridges. *J. Biol. Chem.* **281**, 549–558 (2006).
37. L. S. Gonzalez-Delgado *et al.*, Two-site recognition of Staphylococcus aureus peptidoglycan by lysostaphin SH3b. *Nat. Chem. Biol.* **16**, 24–30 (2020).
38. T. Kaneko, L. Li, S. S.-C. Li, The SH3 domain–A family of versatile peptide- and protein-recognition module. *Front. Biosci.* **13**, 4938–4952 (2008).
39. N. Kurochkina, U. Guha, SH3 domains: Modules of protein-protein interactions. *Biophys. Rev.* **5**, 29–39 (2013).
40. I. Sabala *et al.*, Crystal structure of the antimicrobial peptidase lysostaphin from Staphylococcus simulans. *FEBS J.* **281**, 4112–4122 (2014).
41. T. Uehara, T. Dinh, T. G. Bernhardt, LytM-domain factors are required for daughter cell separation and rapid ampicillin-induced lysis in Escherichia coli. *J. Bacteriol.* **191**, 5094–5107 (2009).
42. N. T. Peters *et al.*, Structure-function analysis of the LytM domain of EnvC, an activator of cell wall remodelling at the Escherichia coli division site. *Mol. Microbiol.* **89**, 690–701 (2013).
43. J. Cook *et al.*, Insights into bacterial cell division from a structure of EnvC bound to the FtsX periplasmic domain. *Proc. Natl. Acad. Sci. U.S.A.* **117**, 28355–28365 (2020).
44. T. Shida, H. Hattori, F. Ise, J. Sekiguchi, Mutational analysis of catalytic sites of the cell wall lytic N-acetylmuramoyl-L-alanine amidases CwlC and CwlV. *J. Biol. Chem.* **276**, 28140–28146 (2001).
45. S. G. Gattis, M. Hernick, C. A. Fierke, Active site metal ion in UDP-3-O-((R)-3-hydroxymyristoyl)-N-acetylglucosamine deacetylase (LpxC) switches between Fe(II) and Zn(II) depending on cellular conditions. *J. Biol. Chem.* **285**, 33788–33796 (2010).
46. B. Kim, A. S. Pithadia, C. A. Fierke, Kinetics and thermodynamics of metal-binding to histone deacetylase 8. *Protein Sci.* **24**, 354–365 (2015).
47. J. E. Cassat, E. P. Skaar, Metal ion acquisition in Staphylococcus aureus: Overcoming nutritional immunity. *Semin. Immunopathol.* **34**, 215–235 (2012).
48. J. Began *et al.*, Rhomboid intramembrane protease YqgP licenses bacterial membrane protein quality control as adaptor of FtsH AAA protease. *EMBO J.* **39**, e102935 (2020).
49. S. Urban, S. W. Dickey, The rhomboid protease family: A decade of progress on function and mechanism. *Genome Biol.* **12**, 231 (2011).
50. P. Rather, Role of rhomboid proteases in bacteria. *Biochim. Biophys. Acta* **1828**, 2849–2854 (2013).
51. G. Liu *et al.*, Bacterial rhomboid proteases mediate quality control of orphan membrane proteins. *EMBO J.* **39**, e102922 (2020).
52. M. K. Lemberg, M. Freeman, Functional and evolutionary implications of enhanced genomic analysis of rhomboid intramembrane proteases. *Genome Res.* **17**, 1634–1646 (2007).
53. Y. Qiao *et al.*, Lipid II overproduction allows direct assay of transpeptidase inhibition by β-lactams. *Nat. Chem. Biol.* **13**, 793–798 (2017).
54. M. A. Welsh *et al.*, Identification of a functionally unique family of penicillin-binding proteins. *J. Am. Chem. Soc.* **139**, 17727–17730 (2017).
55. Y. Rebets *et al.*, Moenomycin resistance mutations in Staphylococcus aureus reduce peptidoglycan chain length and cause aberrant cell division. *ACS Chem. Biol.* **9**, 459–467 (2014).
56. A. J. McCoy *et al.*, Phaser crystallographic software. *J. Appl. Cryst.* **40**, 658–674 (2007).
57. P. D. Adams *et al.*, PHENIX: A comprehensive Python-based system for macromolecular structure solution. *Acta Crystallogr. D Biol. Crystallogr.* **66**, 213–221 (2010).
58. W. Kabsch, XDS. *Acta Crystallogr. D Biol. Crystallogr.* **66**, 125–132 (2010).
59. G. Bunkóczi, R. J. Read, Improvement of molecular-replacement models with Sculptor. *Acta Crystallogr. D Biol. Crystallogr.* **67**, 303–312 (2011).
60. T. C. Terwilliger *et al.*, Iterative model building, structure refinement and density modification with the PHENIX AutoBuild wizard. *Acta Crystallogr. D Biol. Crystallogr.* **64**, 61–69 (2008).
61. P. Emsley, B. Lohkamp, W. G. Scott, K. Cowtan, Features and development of Coot. *Acta Crystallogr. D Biol. Crystallogr.* **66**, 486–501 (2010).
62. P. V. Afonine *et al.*, Towards automated crystallographic structure refinement with phenix.refine. *Acta Crystallogr. D Biol. Crystallogr.* **68**, 352–367 (2012).
63. V. B. Chen *et al.*, MolProbity: All-atom structure validation for macromolecular crystallography. *Acta Crystallogr. D Biol. Crystallogr.* **66**, 12–21 (2010).
64. A. Morin *et al.*, Collaboration gets the most out of software. *eLife* **2**, e01456 (2013).
65. M. Mirdita *et al.*, ColabFold: making protein folding accessible to all. *Nat. Methods.* (2022).
66. G. N. Murshudov, A. A. Vagin, E. J. Dodson, Refinement of macromolecular structures by the maximum-likelihood method. *Acta Crystallogr. D Biol. Crystallogr.* **53**, 240–255 (1997).
67. J. Schindelin *et al.*, Fiji: An open-source platform for biological-image analysis. *Nat. Methods* **9**, 676–682 (2012).
68. M. Kenny, I. Schoen, Violin SuperPlots: Visualizing replicate heterogeneity in large data sets. *Mol. Biol. Cell* **32**, 1333–1334 (2021).
69. J. E. Page, M. A. Skiba, T. Do, A. C. Kruse, S. Walker, 7TJ4. Protein Data Bank. https://www.rcsb.org/structure/unreleased/7TJ4. Deposited 14 January 2022.